Increasing Axial Resolution of Ultrasonic Imaging With a Joint Sparse Representation Model

Junbo Duan, *Member, IEEE*, Hui Zhong, Bowen Jing, Siyuan Zhang, and Mingxi Wan, *Member, IEEE*

***Abstract*— The axial resolution of ultrasonic imaging is confined by the temporal width of acoustic pulse generated by the transducer, which has a limited bandwidth. Deconvolution can eliminate this effect and, therefore, improve the resolution. However, most ultrasonic imaging methods perform deconvolution scan line by scan line, and therefore the information embedded within the neighbor scan lines is unexplored, especially for those materials with layered structures such as blood vessels. In this paper, a joint sparse representation model is proposed to increase the axial resolution of ultrasonic imaging. The proposed model combines the sparse deconvolution along the axial direction with a sparsity-favoring constraint along the lateral direction. Since the constraint explores the information embedded within neighbor scan lines by connecting nearby pixels in the ultrasound image, the axial resolution of the image improves after deconvolution. The results on simulated data showed that the proposed method can increase resolution and discover layered structure. Moreover, the results on real data showed that the proposed method can measure carotid intima–media thickness automatically with good quality (0.56 ± 0.03 versus 0.60 ± 0.06 mm manually).**

***Index Terms*— Carotid intima–media thickness (IMT), deconvolution, sparse representation modeling, ultrasonic imaging.**

I. Introduction

SINCE the discovery of piezoelectric effect by Jacques and Pierre Curie, ultrasound has been widely used in many fields. For example, in medical field, sonography is used to examine the internal structure of human body for diagnosis [1]. In industrial applications, nondestructive testing (NDT) is used to detect the potential flaws in materials [2]. The envelops of sampled signals that are emitted and received by ultrasound transducers are detected using the Hilbert transform. Such B-mode images enable us to investigate the internal acoustic structure of a sample.

However, relatively low resolution limits further application of ultrasonic imaging. The axial (or longitudinal) resolution is defined as a minimum distance that can be differentiated between two reflectors located in the path of an ultrasound beam [3]. The axial resolution is equal to half of the pulse length, which is the product of number of cycles in a pulse and its wavelength. Since transducers and amplifiers have finite bandwidth, the width of the ultrasound pulse generated by the transducer is nonnegligible, and therefore the axial resolution is bounded by this quantity, which is normally in the order of a fraction of a millimeter.

Deconvolution can be used to eliminate the effect of finite bandwidth of an ultrasonic imaging system, and the resolution can be improved significantly [4]–[6]. Deconvolution is the inverse operation of convolution, which models the received signal as a convolutional product of two functions (or signals), one being a reflectivity function and the other being a point spread function (or convolution kernel). The reflectivity function models the acoustic property of test samples, while the point spread function models the overall impulse response of the imaging system.

In linear algebra, the convolution is formulated as the multiplication between a Toeplitz matrix formed from the point spread function and a column vector representing the reflectivity function, which is a sparse vector with spike trains. As a result, the output of deconvolution is the solution of a linear system. There are many regularization terms that can be employed to restore the solution vector, such as the Tukey loss function, Lorentzian loss function, Huber loss function [7], ℓ-(1/2) [8], and ℓ-$p(0 < p < 1)$ [9], [10]. Among them, the ℓ-1 loss function yields a robust and sparse solution [11], [12]. The ℓ-1 loss function is also featured for many interesting theoretical results and computational advantages, such as the restricted isometry property [13], [14], k-step solution property [15], least angle regression [16], and homotopy algorithm [17]. As a result, the ℓ-1 loss function has been intensively studied for ultrasonic imaging [18]–[21].

Restricted by the computational power, most imaging methods deconvolve the data scan line by scan line separately, and the information embedded within the neighbor scan lines is unexplored. Thanks to the modern electronic industry, computational power has improved greatly, which enables us to process the combined data from all scan lines, thereby improving the efficiency.

In this paper, an ℓ-1 norm regularization term is introduced into the basic sparse representation model, which can integrate the information embedded within the neighbor scan lines. The proposed term imposes that the supports of sparse representation vectors of two neighbor scan lines are similar, *i.e.*, the locations of nonzero elements are adjacent. By imposing such a constraint, the temporal concurrency of reflected ultrasonic

Manuscript received May 9, 2016; accepted September 8, 2016. Date of publication September 13, 2016; date of current version December 1, 2016. This work was supported in part by the National Science Foundation of China under Grant 61401352, in part by the China Postdoctoral Science Foundation under Grant 2014M560786, in part by the Shaanxi Postdoctoral Science Foundation, in part by the Fundamental Research Funds for the Central Universities under Grant xjj2014060, and in part by the National Key Research and Development Program of China under Grant 2016YFC0100701. *(Corresponding author: Mingxi Wan.)*

The authors are with the Key Laboratory of Biomedical Information Engineering, Ministry of Education, Department of Biomedical Engineering, School of Life Science and Technology, Xi'an Jiaotong University, Xi'an 710049, China (e-mail: junbo.duan@mail.xjtu.edu.cn; bmezhonghui@mail.xjtu.edu.cn; jingba@stu.xjtu.edu.cn; xjtusyzhang@mail.xjtu.edu.cn; mxwan@mail.xjtu.edu.cn).

Digital Object Identifier 10.1109/TUFFC.2016.2609141

0885-3010 © 2016 IEEE. Translations and content mining are permitted for academic research only. Personal use is also permitted, but republication/redistribution requires IEEE permission. See http://www.ieee.org/publications_standards/publications/rights/index.html for more information.

waveform can be captured, and hence the spatial adjacency of scatters can be explored, which is a characteristic of layered structure such as blood vessels. Since this term accumulates the information of multiple scan lines, the detection of layered structure could be improved. For example, the measurement precision of intima–media thickness (IMT) could be improved. Furthermore, the proposed joint sparse representation model is extended to the complex number domain, and therefore the deconvolution quality can be further improved.

This paper is organized as follows. In Section II, the basic sparse representation model is stated (Section II-A), and then the joint sparse representation model is proposed (Section II-B), and finally it is extended to the complex number domain (Section II-C). The optimization issues related to the proposed model are tackled in Section II-D. The estimation of point spread function is presented in Section III-A, and then the results showing performance of the proposed method using simulations (Section III-B) and real data (Section III-C) including *in vitro* silica gel tube and *in vivo* common carotid artery of a human subject are presented. This paper is concluded in Section IV.

II. Method

A. Basic Sparse Representation Model

The methods presented in [4] and [5] model the received signal of the ith ($i = 1, 2, \ldots, N$) scan line $y_i(t)$ as a linear convolutional product of the reflectivity signal $x_i(t)(i = 1, 2, \ldots, N)$ with a convolution kernel or point spread function $h(t)$, and contaminated with observation noise $n_i(t), (i = 1, 2, \ldots, N)$, where N is the number of transducer array elements.

$\boldsymbol{y}_i$ of length M is used to denote the sampled vector of $y_i(t)$, or the so-called radiofrequency (RF) data, where M is the number of temporal sampling points. Furthermore, $\boldsymbol{Y} = [\boldsymbol{y}_1, \boldsymbol{y}_2, \ldots, \boldsymbol{y}_N]$ is used to denote the RF data set of all scan lines in a frame.

As a result, the convolution model from the linear algebra is as follows:

$$\boldsymbol{y}_i = \boldsymbol{H}\boldsymbol{x}_i + \boldsymbol{n}_i \tag{1}$$

where $\boldsymbol{H}$ is a Toeplitz matrix of size $M \times (M-K+1)$, which is constructed from $h(t)$; K is the support length of the sampled vector of $h(t)$; $\boldsymbol{x}_i$ of length $M - K + 1$ is the sampled vector of the ith reflectivity signal $x_i(t)$; and $\boldsymbol{n}_i$ is a vector with M independent identically distributed (i.i.d.) random variables.

The estimation of $\boldsymbol{x}_i$ from $\boldsymbol{y}_i$ is known as a deconvolution problem. If $h(t)$ is known in advance, then performing the deconvolution is easy. However, in most practical cases, the complete knowledge of $h(t)$ will not be available, *i.e.*, $\boldsymbol{H}$ is an unknown matrix, and therefore both $\boldsymbol{x}_i$ and $\boldsymbol{H}$ have to be estimated together, which is called the blind deconvolution problem [22]. One strategy is to estimate $\boldsymbol{H}$ and $\boldsymbol{x}_i$ jointly [6], and another strategy is to estimate them separately [4], *i.e.*, first $\boldsymbol{H}$ is estimated from $\boldsymbol{Y}$, and then $\boldsymbol{x}$ is estimated based on $\boldsymbol{H}$ [23]. In this paper, the second strategy is used, and the estimation of $\boldsymbol{H}$ is presented in Section III-A.

Now we assume that $\boldsymbol{H}$ is known, based on (1) and the assumption that $\boldsymbol{n}_i$ follows a Gaussian distribution, the least square solution of $\boldsymbol{x}_i$ is $\boldsymbol{H}^+\boldsymbol{y}_i$, where $\boldsymbol{H}^+ = (\boldsymbol{H}^T\boldsymbol{H})^{-1}\boldsymbol{H}^T$ is the MoorePenrose pseudoinverse of $\boldsymbol{H}$ and ^{T} denotes the transpose operation. Since the condition number of Toeplitz matrix $\boldsymbol{H}$ is very large, the least square solution is ill-posed, yielding limited resolution in the deconvolved image [24], so an ℓ-1 norm regularization term is added as a remedy.

The ℓ-1 norm regularized least square estimator of $\boldsymbol{x}_i$ is known as basis pursuit denoising (BPDN) [24], and is expressed as

$$\hat{\boldsymbol{x}}_i = \arg\min_{\boldsymbol{x}_i} \|\boldsymbol{y}_i - \boldsymbol{H}\boldsymbol{x}_i\|^2 + \lambda_x \|\boldsymbol{x}_i\|_1 \tag{2}$$

where $\|\cdot\|$ and $\|\cdot\|_1$ denote the ℓ-2 and ℓ-1 norm, respectively, and λ_x is a regularization parameter that controls the tradeoff between the first and second terms, *i.e.*, fitting fidelity and sparsity, respectively. Large λ_x encourages $\boldsymbol{x}$ with high sparsity level, *i.e.*, more zero elements in $\boldsymbol{x}$, and strong noise suppression, and vice versa.

It should be noted that BPDN is equivalent to the famous estimator LASSO [11], [25], [26], and therefore the numerical tools that are designed for LASSO can be applied to BPDN. Using BPDN repeatedly on each scan line $\boldsymbol{y}_i$, one can restore a deconvolution image $\hat{\boldsymbol{X}} = [\hat{\boldsymbol{x}}_1, \hat{\boldsymbol{x}}_2, \ldots, \hat{\boldsymbol{x}}_N]$ of size $(M - K + 1) \times N$ (without zero padding), which has higher resolution compared with image $\boldsymbol{Y}$. Since the ℓ-2 and ℓ-1 norms of a matrix can be decoupled column-wise, N BPDN optimization problems can be encompassed in a unified equivalent optimization form as follows:

$$\hat{\boldsymbol{X}} = \arg\min_{\boldsymbol{X}} \|\boldsymbol{Y} - \boldsymbol{H}\boldsymbol{X}\|^2 + \lambda_x \|\boldsymbol{X}\|_1. \tag{3}$$

B. Joint Sparse Representation Model

The above basic sparse deconvolution model does not consider any neighborhood information, *i.e.*, information embedded within neighbor scan lines. Suppose that a layered structure shows up horizontally in the observed region (for example, refer to the top-left panel of Fig. 1), then the echogenic waves should appear in neighbor RF data $\boldsymbol{y}_j$ and $\boldsymbol{y}_{j+1}$ simultaneously (*i.e.*, with the same time delay). Furthermore, spikes should appear at the same loci in the corresponding deconvoluted signals $\boldsymbol{x}_j$ and $\boldsymbol{x}_{j+1}$, *i.e.*, $i+1$th locus of both $\boldsymbol{x}_j$ and $\boldsymbol{x}_{j+1}$, yielding $x_{i+1,j} = x_{i+1,j+1}$. This characteristic can be extracted as prior knowledge to improve the quality of deconvolution in terms of axial resolution [27]. When the layered structure is not strictly horizontal but with a slight rotation, then there is a time shift between the two echogenic waves of neighbor RF data. This results in a slight shift in the spikes of $\boldsymbol{x}_j$ and $\boldsymbol{x}_{j+1}$. As a result, we no longer have $x_{i+1,j} = x_{i+1,j+1}$ but $x_{i,j} = x_{i+1,j+1}$ or $x_{i+1,j} = x_{i,j+1}$, depending on the slope of the layer (for example, refer to the rest corner panels of Fig. 1).

We borrow the idea of total variation method [28], which is frequently used in image processing community for robust denoising by exploring the information from the neighborhood. Here a similar regularization term is proposed to regularize the solution $\boldsymbol{X}$

$$P(\boldsymbol{X}) = \sum_{i=1:M-K, j=1:N-1} |x_{i,j} + x_{i+1,j} - x_{i,j+1} - x_{i+1,j+1}|. \tag{4}$$

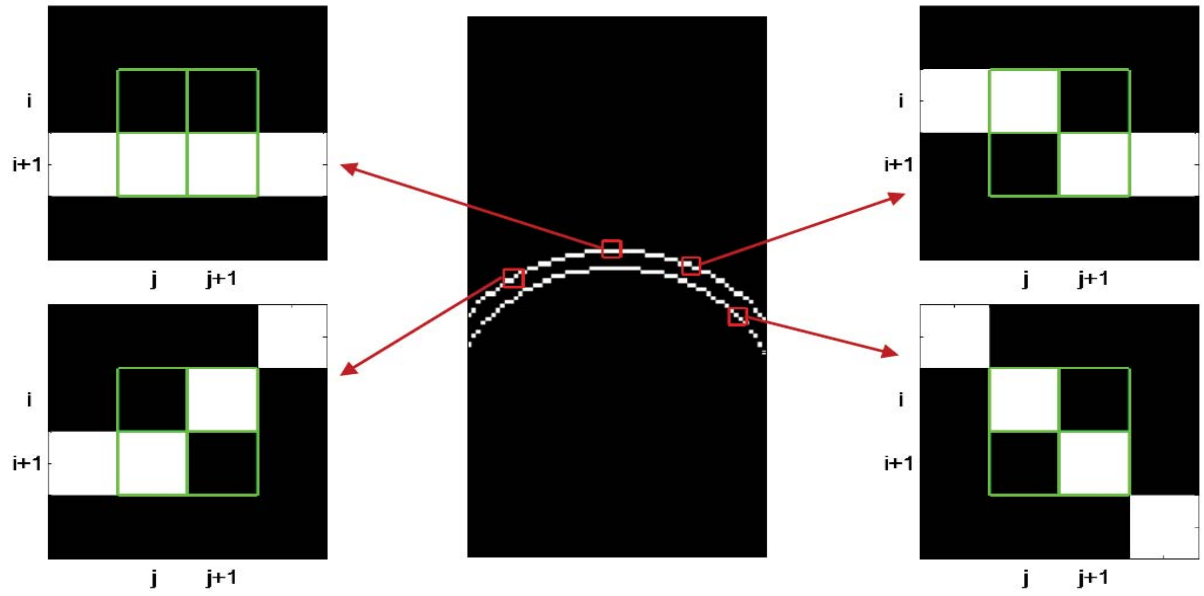

Fig. 1. Schematic of the proposed regularization term $P(\boldsymbol{X})$ in (4). The central panel shows the imaging region with two layers. Corner panels are zoomed-in view of four typical four-connected neighborhood on a layer, with regularization term $x_{i,j}+x_{i+1,j}-x_{i,j+1}-x_{i+1,j+1}=0$. Black and white encode 0 and 1.

This term encourages the concurrence of echogenic waves of neighbor scan lines. Suppose that there is a spike at locus $x_{i,j}$ or $x_{i+1,j}$, then this term expects a spike at locus $x_{i,j+1}$ or $x_{i+1,j+1}$ with the same amplitude. By checking the four corner panels as shown in Fig. 1, one can see that (4) equals to zero. Therefore, this term can be employed to detect the layered structure with any slight slope. It should be noted that the regularization term is equivalent to a 2×2 operator $\begin{bmatrix}1 & -1\\ 1 & -1\end{bmatrix}$, which is different from a one-directional gradient kernel $[\,1\ -1\,]$. The former operator can capture all the four corner panels of Fig. 1, while the latter can capture only the top-left one.

By adding this regularization term into (3), the joint sparse representation model in matrix form reads as follows:

$$\hat{\boldsymbol{X}}=\arg\min_{\boldsymbol{X}}\|\boldsymbol{Y}-\boldsymbol{H}\boldsymbol{X}\|^2+\lambda_x\|\boldsymbol{X}\|_1+\lambda_p P(\boldsymbol{X}) \tag{5}$$

where λ_p is the second regularization parameter that can control the tradeoff among fitting fidelity, overall sparsity, and layered structure sparsity.

C. Joint Sparse Representation Model in Complex Number Domain

Model (5) considers only the real number, *i.e.*, elements of $\boldsymbol{Y}$ and $\boldsymbol{H}$ take real values. As a result, the elements of solution $\hat{\boldsymbol{X}}$ take real values, which contain only the amplitude information of reflectivity function, and the phase information is missing. The estimated time delay of waveform is discretized and takes only the value on the temporal sampling grids.

To improve the estimation of time delay, the model is extended to complex number domain, *i.e.*, elements of $\boldsymbol{X}$ are defined on complex number domain and become phasors. Therefore, the RF data $\boldsymbol{Y}$ and convolution kernel matrix $\boldsymbol{H}$ have to be extended to the complex number domain.

We employ the discrete Hilbert transform to compute analytic signals of both $\boldsymbol{Y}$ and $\boldsymbol{H}$ column by column. As a result, the joint sparse representation model for complex number domain is given as follows:

$$\hat{\boldsymbol{X}}=\arg\min_{\boldsymbol{X}}\|\mathcal{H}\{\boldsymbol{Y}\}-\mathcal{H}\{\boldsymbol{H}\}\boldsymbol{X}\|^2+\lambda_x\|\boldsymbol{X}\|_1+\lambda_p P(\boldsymbol{X}) \tag{6}$$

where $\mathcal{H}$ is the discrete Hilbert transform operator [29]. The solution $\boldsymbol{X}$ is now defined in the complex number domain.

D. Optimization and Implementation Issue

It should be noted that one cannot find a linear operator of $\boldsymbol{X}$ to formulate the second regularization term in (6), and therefore, efficient linear optimization solvers cannot be used to tackle the joint sparse representation model. However, if $\boldsymbol{X}$ is reshaped as a vector $\tilde{\boldsymbol{x}}$ by cascading the columns, a sparse matrix operator $\tilde{\boldsymbol{P}}$ of size $(N-1)(M-K)\times(M-K+1)N$ can be constructed such that $\|\tilde{\boldsymbol{P}}\tilde{\boldsymbol{x}}\|_1=P(\boldsymbol{X})$. The elements of $\tilde{\boldsymbol{P}}$ are defined as

$$\tilde{p}_{i,j}=\begin{cases}-1, & i=(\alpha-1)(M-K)+\beta\\ & j=(\alpha-1)(M-K+1)+\beta+\{0,1\}\\ 1, & i=(\alpha-1)(M-K)+\beta\\ & j=\alpha(M-K+1)+\beta+\{0,1\}\\ 0, & \text{else}\\ & (\alpha=1,2,\ldots,N-1;\ \beta=1,2,\ldots,M-K).\end{cases} \tag{7}$$

Finally, the joint sparse representation model is given as follows:

$$\hat{\tilde{\boldsymbol{x}}}=\arg\min_{\tilde{\boldsymbol{x}}}\|\tilde{\boldsymbol{y}}-\tilde{\boldsymbol{H}}\tilde{\boldsymbol{x}}\|^2+\lambda_x\|\tilde{\boldsymbol{x}}\|_1+\lambda_p\|\tilde{\boldsymbol{P}}\tilde{\boldsymbol{x}}\|_1 \tag{8}$$

where $\tilde{\boldsymbol{y}}$ of length MN is the vectorized version of $\mathcal{H}\{\boldsymbol{Y}\}$ by cascading all the columns; $\tilde{\boldsymbol{H}}$ of size $MN \times (M-K+1)N$ is a block diagonal matrix defined as $\tilde{\boldsymbol{H}} = \boldsymbol{I}_N \otimes \mathcal{H}\{\boldsymbol{H}\}$, where $\boldsymbol{I}_N$ of size $N \times N$ is an identity matrix; and $\otimes$ is the Kronecker product operator.

It should be noted that both $\tilde{\boldsymbol{H}}$ and $\tilde{\boldsymbol{P}}$ are huge matrices, and need large memory to store them. For example, if $M = 1000$, $N = 128$, and $K = 50$, then the memory required to store the full form of $\tilde{\boldsymbol{H}}$ is 116 GB. The sparsity of matrices is advantages, and therefore can be stored in sparse form.

It can be noted from (8) that all the three terms are convex with respect to $\tilde{\boldsymbol{x}}$, therefore the optimization criterion is convex, and any standard numerical optimization tools designed for convex programming can be used to solve this problem. In this paper, we used the MATLAB package CVX [30], [31], which is a modeling system for constructing and solving disciplined convex programs.

III. Results

In this section, first, SonixTOUCH is used to acquire RF data sampled at 40 MHz, and the nominal central frequency of probe is 5 MHz. Then the acquired RF data are used to estimate the point spread function $h(t)$ by fitting the observed power spectrum with Gaussian functions. Furthermore, simulations were carried out based on the estimated point spread function $h(t)$ to demonstrate the performance of the proposed method. The best setting for regularization parameters λ_x and λ_p for real data processing, which includes the data of a silica gel tube and a common carotid artery, is determined based on simulations.

A. Estimation of Point Spread Function

The point spread function $h(t)$ is estimated from the real data with the following steps.

1) The power spectrum of each scan line is calculated using a fast Fourier transform.
2) The mean spectrum of all the scan lines is calculated to remove the measurement noise.
3) The observed spectrum, *i.e.*, the mean spectrum is fitted with a linear combination of Gaussian functions to further remove the noise and distortion caused by the nonlinear response of tissues. The least square error of the fitting result and the observed spectrum is used to measure the quality of curve fitting. Here, the three parameters to be estimated for each Gaussian function are the amplitude, center location, and standard deviation. Three Gaussian functions are used since biological tissues can introduce both subharmonic and superharmonic. The first, second, and third (according to the center location) Gaussian components correspond to the subharmonic, fundamental, and superharmonic components, respectively. Since the optimization criterion is not convex with respect to the parameters, local minima are inevitable. As a result, the optimization is sensitive with respect to the initial point. The central frequency is initialized with 2.5, 5, and 7.5 MHz; the amplitude to be half, one, and half of the maximum of the mean spectrum; and the standard deviation to be $0.6 \times 5 = 3$ MHz.

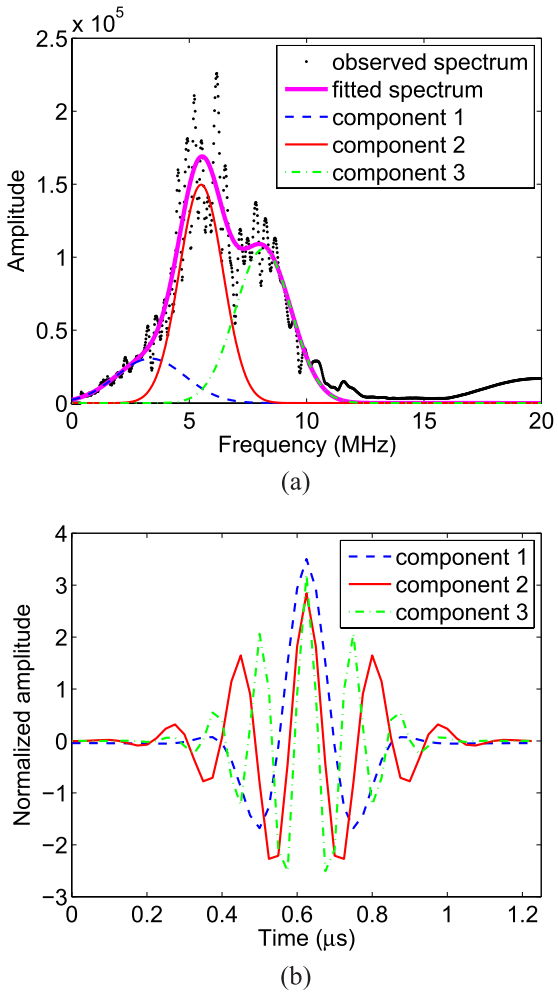

Fig. 2. Estimation of point spread function $h(t)$ from silica gel tube data set. (a) Fitting result of the observed power spectrum with three Gaussian functions. (b) Estimates of three component waveforms after normalization.

4) The second Gaussian component is transformed from frequency domain to temporal domain, and retained the central $K = 50$ points to cover the support of the point spread function [$50 \gg (40/5$ MHz)].
5) The resultant waveform is normalized such that the standard deviation is equal to one.

The fitting results are displayed in Fig. 2. The black dotted curve in (a) is the observed spectrum, whereas the magenta solid curve is the fitted spectrum, with three Gaussian functions colored in blue, red, and green as the components.

It should be noted that the nominal pulse central frequency of probe is 5 MHz, but the estimated central frequency of the second component is 5.4 MHz, which improves the deconvolution performance. It can be noted that the central frequency of the first and third components is about 0.5 and 1.5 times that of the second component, and therefore the corresponding harmonics are of $(1/2)$ and $(3/2)$ order, respectively.

The three components are displayed in Fig. 2(b). In the following studies, the second component (with $K = 50$) is used as the point spread function in the deconvolution.

B. Simulation Studies

The aim of the simulation studies is twofold: 1) to test the performance of the proposed method and 2) to search the best

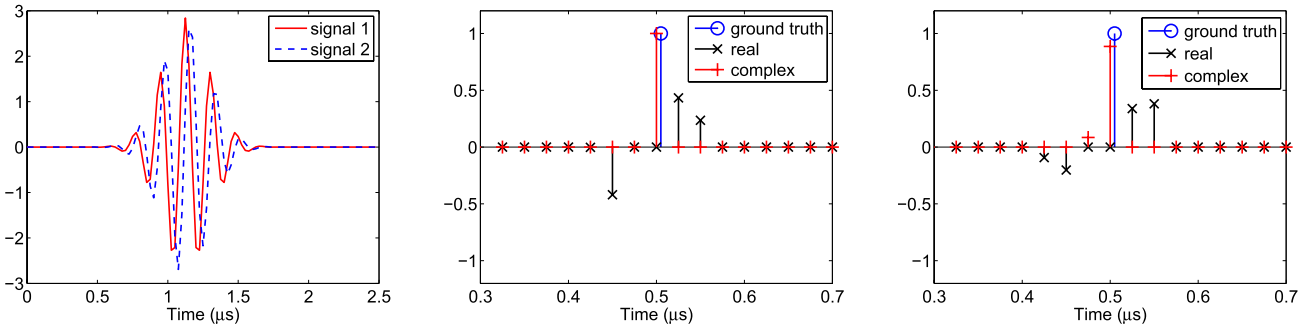

(a) (b) (c)

Fig. 3. Simulation study I. (a) Simulated noiseless signals 1 and 2; the former signal starts at 0.5 μs, and the latter is 0.005 μs delayed of the former. (b) and (c) Deconvolution results with noise level $\sigma = 0$ and 0.3, corresponding to noiseless and noisy scenario, respectively.

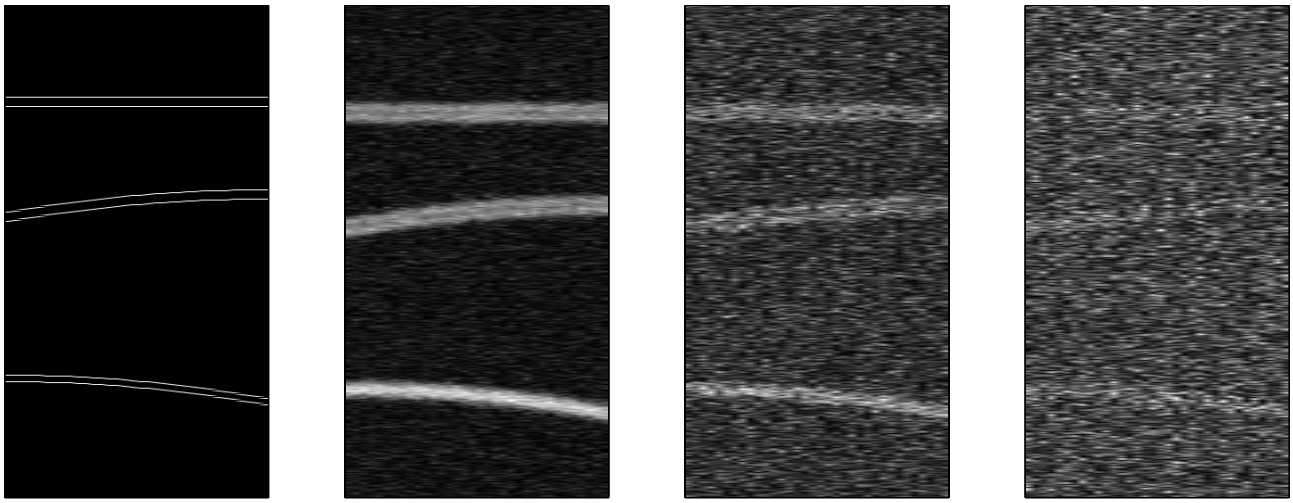

(a) (b) (c) (d)

Fig. 4. Simulation study II. (a) Ground true image with three tubes; the inside diameters from top to bottom are 9, 9, and 6 pixels. (b)–(d) B-mode images of simulated RF data with noise level $\sigma = 0.3$, 1, and 2, respectively, corresponding to high, moderate, and low data quality scenario.

setting for regularization parameters λ_x and λ_p for real data analysis. To make the setting applicable for real data analysis, both $\tilde{\boldsymbol{y}}$ and $\tilde{\boldsymbol{h}}$ were normalized to have zero mean and unit standard deviation before calling CVX in the simulation study.

1) Simulation I: The first simulation aims to compare the deconvolution performance of the real number model with that of the complex number model. First, two noiseless echogenic signals were simulated, with starting point at 0.5 and 0.505 μs [signals 1 and 2 in Fig. 3(a)]. Since the sampling frequency is 40 MHz, the temporal span between two consecutive RF sample points is 0.025 μs. Therefore, the former signal aligns to the sampling grid strictly, but the latter has an indentation of 0.2 (=0.005/0.025) unit of sampling interval. Then signal 2 was deconvolved with both real number model and complex number model. The deconvolution results are shown in Fig. 3(b). The ideal deconvolution result should be a spike at location 0.505 μs [the ground truth, blue circle in Fig. 3(b)], but this location is not on the sampling grid. Using the real number model, the ground truth spike splits into several smaller spikes around (black crosses). As a comparison, the result with complex number model (red pluses) approximates the ground truth well. Fig. 3(c) shows the deconvolution results with noise level $\sigma = 0.3$. It is shown that the results degenerate with both models compared with the noiseless scenario, but the result with complex number model is still superior to that with real number counterpart.

2) Simulation II: In the second simulation, first, an image $\boldsymbol{X}$ of 1×1 cm (532×34 pixels) is generated as the ground truth [refer to Fig. 4(a)], which includes three tubes with inside diameter 9, 9, and 6 pixels from top to bottom. Since each pixel represents a sample point, and 40 MHz is used as the sampling frequency, the corresponding inside diameters of the three tubes are 173.25, 173.25, and 115.5 μm, respectively. The width of the tube wall is 1 pixel. The top tube is strictly straight and horizontally placed, while the bottom two tubes are bent slightly. Considering tube width and curvature, the recovery difficulty increases from the top tube to the bottom one.

The estimated point spread function [component 2 in Fig. 2(b)] is used to simulate the sampled RF data. To simulate the measurement noise and system error, a random noise that obeys i.i.d. Gaussian distribution with zero mean is added. The standard deviation σ takes three values: 0.3, 1, and 2, which correspond to high, moderate, and low data quality scenarios, respectively. The B-mode images of these three scenarios are displayed in Fig. 4(b)–(d). It can be seen from Fig. 4(b) that the top two tubes are hollow, while the bottom one is solid. The three tubes are clearly visible,

but there seems no difference among them in Fig. 4(c). When the noise level is high, the three tubes are difficult to recognize in Fig. 4(d). In summary, the low resolution of the images is caused by the presence of noise and the width of the point spread function.

To achieve the best performance of the proposed method, the regularization parameters λ_x and λ_p have to be tuned to their best setting. A 2-D grid search was used to tune the regularization parameters, *i.e.*, both $\log_{10}\lambda_x$ and $\log_{10}\lambda_p$ were assigned values from -4 to -0.5 with a step length of 0.5 (totally eight values). The corresponding optimization problem was solved for each combination of λ_x and λ_p, and the recovery error was calculated. Ten Monte Carlo replicates were generated, and the obtained recovery errors were averaged. After the errors of all possible combinations ($8 \times 8 = 64$) were calculated, the setting of λ_x and λ_p that yields the lowest recovery error ϵ was chosen as the best setting. The recovery error is defined as the normalized root of least square error $\epsilon = ((\|\hat{\tilde{\boldsymbol{x}}} - \tilde{\boldsymbol{x}}\|)/(\|\tilde{\boldsymbol{x}}\|))$.

The results of 2-D grid search for the high data quality scenario are shown in Fig. 5(a), and it is found that the best settings for λ_x and λ_p are 0.1 and 0.01, respectively. The recovered image with the best setting is shown in Fig. 5(d). It can be observed that the recovery is perfect. To compare the obtained results with basic recovery method, the proposed regularization term is disabled by setting the parameter λ_p to zero, and the recovered image is shown in Fig. 5(g). It can be seen from Fig. 5(g) that the recovered image after disabling the parameter λ_p is clear, but the walls of the bottom tube are not smooth. This is due to the presence of noise and measurement error in the data, which leads to the wrong detection of layer location, *i.e.*, a few points ahead or behind the true one, yielding nonsmoothness of the tube wall. The proposed method utilizes the neighborhood information by the additional regularization term to connect neighbor layer loci, yields robust estimation of the layer location, and therefore improves the image quality.

The results of moderate data quality scenario are shown in Fig. 5(b), (e), and (h), which shows that the best setting for λ_x and λ_p is 0.03 and 0.01, respectively. For the proposed joint sparse method [Fig. 5(e)], the recovery result of the top two tubes is good, but the bottom one has some false layers, which is due to the fact that the inside diameter of the bottom tube is much smaller than that of the top two. While for the basic method, all three tubes have strong false layers [Fig. 5(h)].

For the low data quality scenario, the best setting of λ_x and λ_p is 0.03. It is shown that the basic method can hardly recover any of the three tubes [Fig. 5(i)], but the proposed method can recover all three tubes [Fig. 5(f)], and the two walls of the top tube are clearly detected.

From Fig. 5(a)–(c), it can be observed that when the data quality is poor, the best setting of λ_x decreases, while that of λ_p increases. This could be employed as the general rule for regularization parameter selection.

C. Real Data Analysis

In the experiments, the SonixTOUCH system of Ultrasonix was used to acquired RF data. The probe is a 38-mm linear array with 128 elements. The maximum depth was set to 40 mm. Pulse mode was used with a central frequency of 5.4 MHz and duration period one cycle. The RF sampling frequency is 40 MHz.

Two sets of real data were obtained and processed. The first data set is *in vitro*, which was sampled on a silica gel tube, and the second one is *in vivo*, which was sampled on a common carotid artery of a human subject.

1) In Vitro Experiment: The tube is made of silica gel with outer and inner diameters of 1.8 and 1 mm, respectively. The tube was immersed in a tank with degassed water while imaging. The lumen of the right end of the tube was filled with water, while that of the left end was empty (with air). The tube was inclined slightly to increase the recovery difficulty. The experiment was conducted in normal indoor temperature.

It was observed from the simulation studies that the best setting of λ_x and λ_p is within 0.1 and 0.01, which can be used in the real data analysis. However, the applicability depends on the condition that the scale of the data should be comparable. In the simulation, the scales of $\tilde{\boldsymbol{y}}$ and $\boldsymbol{h}$ are normalized to have zero mean and unit standard deviation. Thus, $\tilde{\boldsymbol{y}}$ and $\boldsymbol{h}$ were also normalized in the real data analysis as well.

For the silica gel tube data set, it was found that the best parameter values to process this set are $\lambda_x = \lambda_p = 0.11$. The results are presented in Fig. 6. The system b8 image, B-mode image of the RF data with Hilbert transform, reconstructed result of the basic sparse deconvolution, and that of the proposed method are shown in Fig. 6(a)–(d), respectively. Since there are four interfaces, *i.e.*, two inside and two outside interfaces, four layers are clearly detected as the top four layers of the right end (with water inside). It should be noted that the bottom layer is an artifact caused by reverberation, which will be discussed in detail in Section IV.

Compared with the results without deconvolution [Fig. 6(a) and (b)], Fig. 6(c) and (d) show that the thickness of the layers decreased significantly, indicating that the lateral resolution of the ultrasonic imaging is greatly increased by deconvolution. Moreover, compared with basic deconvolution method [as shown in Fig. 6(c)], Fig. 6(d) shows the advantage of the proposed joint sparse representation model, *i.e.*, independent small dashes and dots in Fig. 6(c) are either filtered out or connected together to form long strings, which is due to the regularization term in (4).

Normalized autocorrelation function is commonly employed to qualitatively study the resolution of an image [6], [32], [33]. For each scan line, the autocorrelation function is defined as the inner product of the vector of the scan line and the axially shifted version of the vector. The autocorrelation function is then normalized by its ℓ_2-norm and averaged across all scan lines within the region without water inside. Fig. 6(e) displays the autocorrelation function of Fig. 6(a)–(d). It is shown that for the autocorrelation functions of Fig. 6(c) and (d), the peaks at shift distance zero are very sharp, indicating superior resolution. It can be observed from the markers on the red curve in Fig. 6(e) that the thickness of the tube is 1.81 mm, which is consistent with the measurement by vernier caliper (1.8 mm).

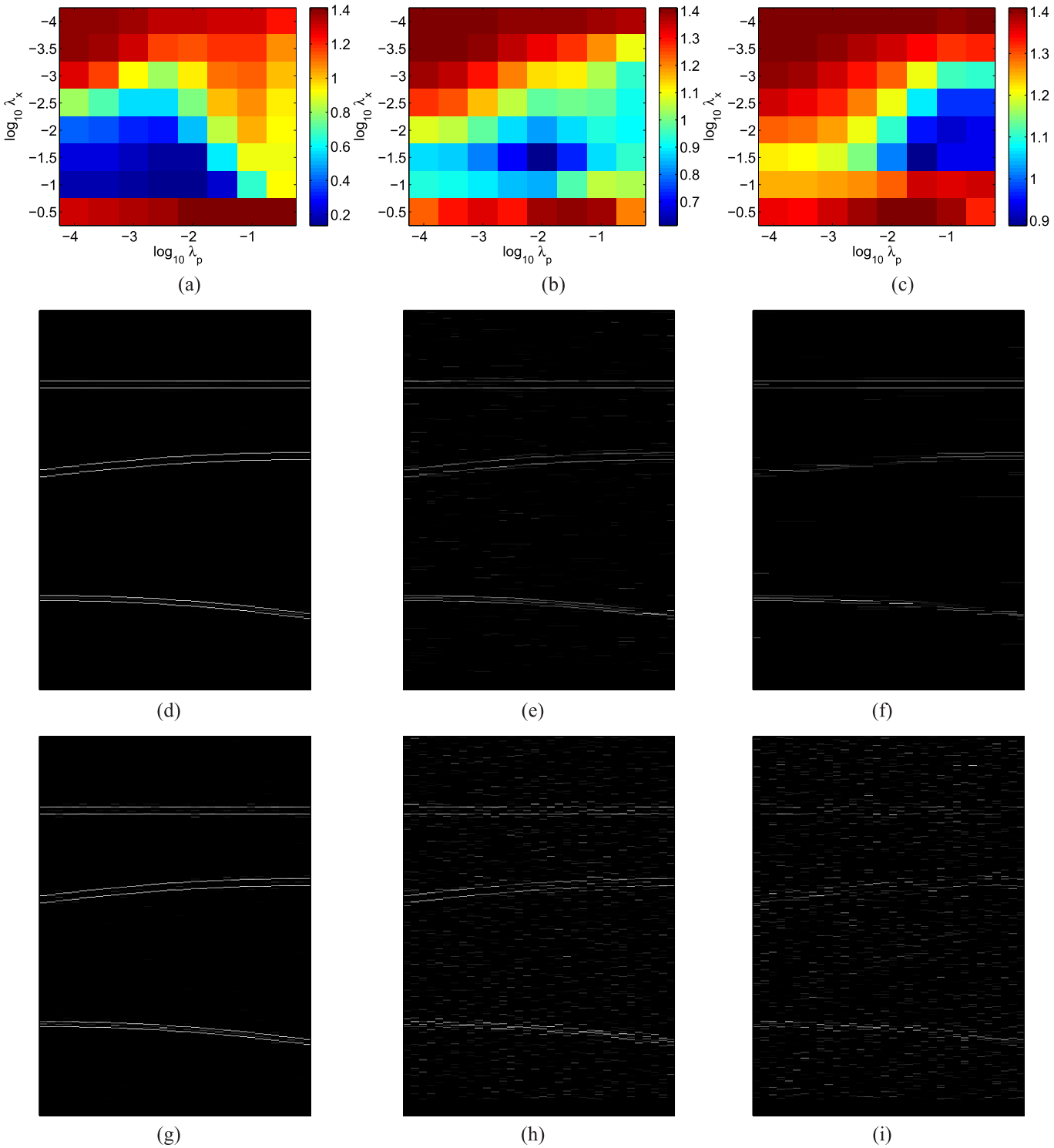

Fig. 5. Left ((a), (d), and (g)), middle ((b), (e), and (h)), and right ((c), (f), and (i)) columns show the simulation results with high, moderate, and low data quality scenario, respectively. The best settings of λ_x and λ_p are (0.1, 0.01), (0.03, 0.01), and (0.03, 0.03). The top ((a), (b), and (c)), middle ((d), (e), and (f)), and bottom ((g), (h), and (i)) rows show the recovery error with respect to parameters λ_x and λ_p, the recovery result with the proposed joint sparse representation model (with the best parameter setting), and the result with basic method (with $\lambda_p = 0$).

Besides the peak at shift distance zero with amplitude one, there are three peaks at shift distances of 0.56, 1.81, and 2.37 mm. The peak at a shift distance of 0.56 mm corresponds to the inner production when the second layer from the top is shifted and overlaps with the top one. Similarly, peak at 1.81 mm corresponding to the second layer from the bottom overlaps with the top one, and peak at 2.37 mm corresponding to the bottom layer overlaps with the top one. It should be noted that the peak corresponding to the middle layer that overlaps with the top one is absent, but there are two split plateaus at shift distances of 0.9 and 1.3 mm.

Since this data set has near-perfect layers, besides utilizing the autocorrelation function, one can study the resolution directly. During experiments, we selected the profile of the

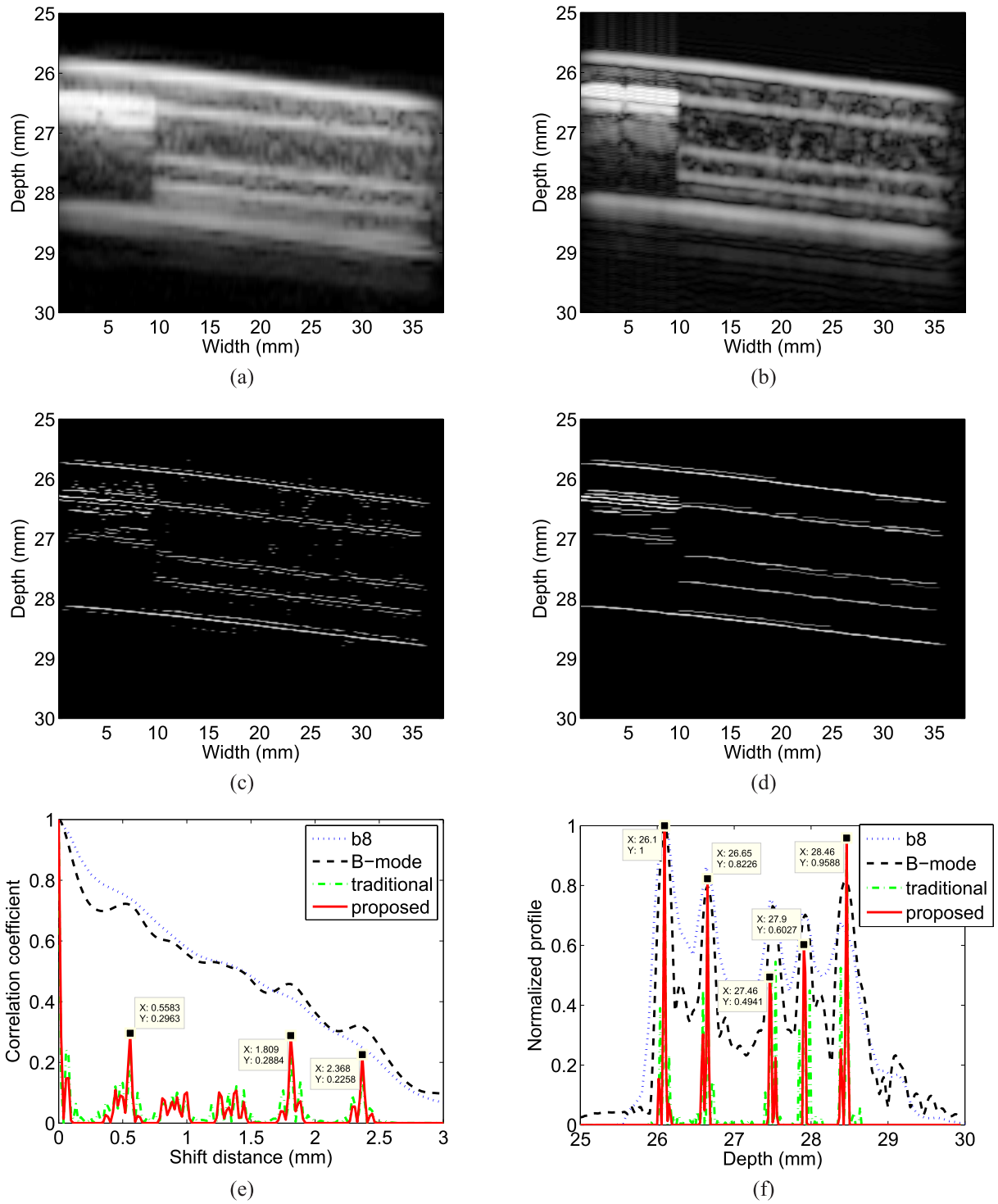

Fig. 6. Experimental results of the region of interest of the silica gel tube. (a)–(d) System b8 image, B-mode image of the RF data, reconstruction image of the basic sparse deconvolution, and of the proposed method, respectively. (e) and (f) Autocorrelation function and normalized profile of the lateral view of the above four images.

middle scan line (width = 19 mm), aligned the profiles of other scan lines to this selected one, averaged all profiles, and finally normalized the profiles such that the largest value is equal to one. Fig. 6(f) shows the normalized profiles of each image. It can be seen from the results that the images processed by the proposed method has the best resolution, followed by the deconvolution image, the B-mode RF image, and the system b8 image. It is also shown that the thickness of the top and bottom walls and the lumen diameter are 0.55, 0.44, and 0.81 mm, respectively. It should be noted that the first four peaks correspond to the four interfaces of the tube, the last one is an artifact caused by reverberation, and details of which will be discussed in Section IV.

In summary, the results show that the proposed method can discover layered structure with high axial resolution compared with B-mode method and basic sparse representation method.

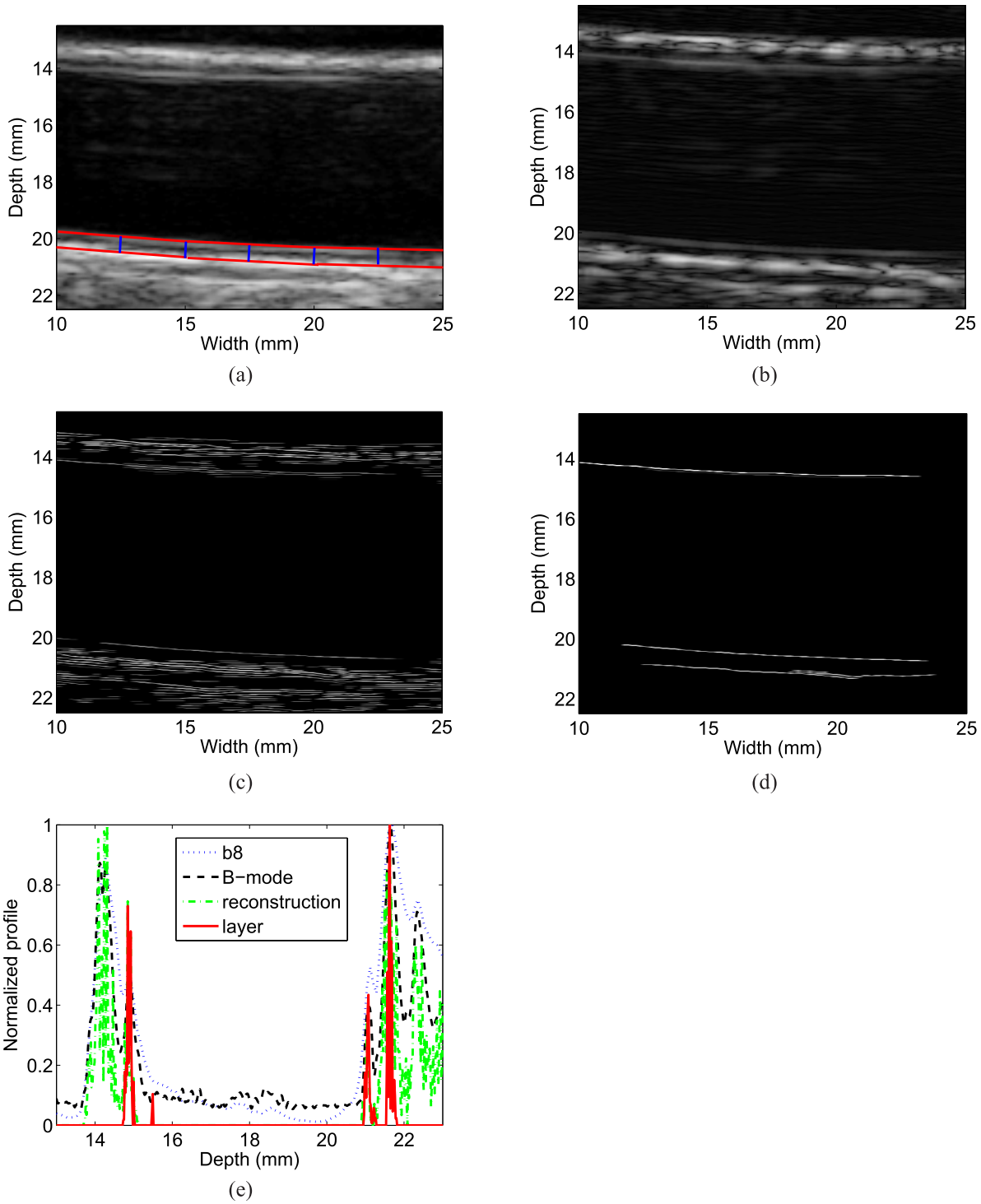

Fig. 7. Zoomed-in view of the region of interest of the common carotid artery real data set. (a) System b8 image. (b) B-mode image of RF data. (c) Reconstruction image with the proposed method. (d) Discovered layers of the artery. (e) Normalized profile of the lateral view of the above four images.

2) In Vivo Experiment: The IMT is a measurement of thickness of two of the innermost layers of an artery wall, *i.e.*, the thickness of the tunica intima and tunica media [34]. The carotid IMT (cIMT) is usually employed to track the changes of carotid artery and to predict and detect the presence of plaques and atherosclerotic disease in early stage. The average cIMT of a healthy individual is 0.4 mm by birth and 0.8 mm by the age of 80 [35]. With the increase in cIMT, the cardiovascular risk increases more rapidly over a lifetime. Therefore, as a noninvasive and cost-efficient measurement, cIMT is an important surrogate marker for cardiocerebrovascular studies.

The precise and automatic measurement of cIMT is challenging because of the low resolution of ultrasound imaging.

In this experiment, the proposed joint sparse representation model is employed to achieve accurate measurement of cIMT. The common carotid artery data of a healthy individual are sampled for this study, and the corresponding results are depicted in Fig. 7. The SonixTOUCH system b8 image and the B-mode image of the sampled RF data are shown in Fig. 7(a) and (b), respectively. It can be seen that there are two lines in both far (deeper) wall and near (shallower) wall, corresponding to the lumen–intima interface and the media–adventitia interface [34]. The latter is seen as the thin layers at a depth of around 14 and 20 mm, which is much thinner and weaker than the former.

This data set was processed the same way as the silica gel tube data set mentioned previously, *i.e.*, the same point spread function was used and the signals were normalized following the same procedure. Since the biological tissues have nonlinear effects, and also the tunica intima signal is much weaker than that of the other tissues, smaller regularization parameters $\lambda_x = 0.06$ and $\lambda_p = 0.01$ were used. The reconstruction image with the proposed method is shown in Fig. 7(c), which consists of several small segments. To detect the layers of cIMT, the eight-connected objects are labeled first (which are encouraged by the proposed regularization term (4)), and then these objects are sorted according to their length and preserved the longest layers whose width is less than 10 pixels. The filtered results are shown in Fig. 7(d), in which three were left. The results from top to bottom correspond to the intima–lumen interface of the near wall, the intima–lumen and adventitia–media interface of the far wall. The measured cIMT from far wall is 0.56 ± 0.03 mm. As a comparison, the cIMT from the system b8 image was also measured manually. First, we drew the profiles of intima and media layer [the two red lines in Fig. 7(a)], and then five equally spaced thicknesses (the five blue lines) were measured, yielding cIMT measurement of 0.60 ± 0.06 mm. Fig. 7(e) shows the resolution profiles of Fig. 7(a)–(d), and it is shown that the three layers have sharp peaks in the profiles, indicating superior resolution of the proposed method.

It is also worthy to note that in Fig. 7(d), two layers are detected at the far wall, but only one layer is detected at the near wall. This is because the strength of echogenic wave is lost when the beam travels from more echogenic to less echogenic layers at the adventitia–media interface of the near wall. Previous studies recommended far wall rather than near wall to increase the sensitivity and accuracy of cIMT measurement [36], which is consistent with our observation.

3) Computational Burdens: The probe has 128 elements, the maximal depth is 40 mm, and the RF sampling frequency is 40 MHz, and therefore the acquired RF data set is 2080 by 128 matrices ($2080 \approx ((40\text{ mm} \times 2)/(1540\text{ m/s})) \times 40$ MHz).

We used MATLAB of MathWorks to implement the proposed method, and ran codes on a desktop with Intel i7 processor and 32 GB memory. As discussed earlier in Section II-D, since $\tilde{\boldsymbol{H}}$ is a huge matrix, the processing of whole data set led to error "out of memory." Therefore, the image is divided vertically into two parts ($M = 1040$) and each part is processed separately. The processing of each part cost approximately 6 min and 9 GB memory space.

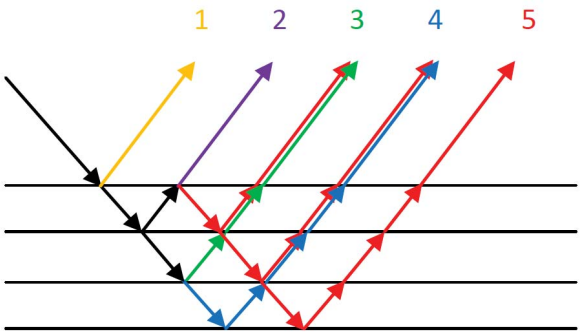

Fig. 8. Demonstration of the echogenic waves of silica gel tube data set. The first four echogenic waves are reflected by the four interfaces of the tube, and the fifth is an artifact caused by reverberation (red lines).

IV. Conclusion

A joint sparse representation model to increase the axial resolution of ultrasonic imaging is presented in this paper. Both simulation and real data studies supported the effectiveness of the proposed method. The main contributions are twofold.

1) The proposed method has an additional regularization term, which can integrate the information of echogenic waves from neighbor scan lines. This feature enables the combined processing of the RF data of all scan lines of a frame, and hence improves the axial resolution to a greater extent compared with the conventional methods, which process the RF data scan line by scan line separately.
2) From the application point of view, since the additional regularization term encourages the connectivity of pixels along the lateral direction, the proposed method is appropriate to discover layered structure. Some of the potential examples are the measurement of IMT in clinical medicine and the measurement of coating thickness of printed circuit board in NDT.

It should be noted that in the silica gel tube experiment, since there are four interfaces, *i.e.*, two inside and two outside interfaces, four layers should be in the ultrasound image. However, as shown in Fig. 6, there are five layers. The top four layers correspond to the four interfaces of the tube, while the bottom one is caused by reverberation, and is highlighted in red in Fig. 8. It can be observed from Fig. 8 that the wave path difference between waves 1 and 2 is the same as the one between waves 4 and 5 (about double the thickness of the tube wall). This is in agreement with the fact that in Fig. 6(e) and (f), the difference between the first two peaks [0.558 in Fig. 6(e) and 0.55 in Fig. 6(f)] is the same as the difference between the last two peaks [0.559 in Fig. 6(e) and 0.56 in Fig. 6(f)].

The main limitation of this paper is that the estimated point spread function used for deconvolution does not match consistently with the RF signals. Consequently, there are side lobes in the deconvolved images [see Fig. 6(e) and (f)]. To overcome this impairment, the advanced convolution kernel should be considered. For example, in the current convolution model, the convolution kernel is invariable. However, because of attenuation and dispersion that cause distortion in spectrum,

the waveform changes with respect to travel distance [21]. Therefore, a variable convolution kernel should be considered.

The selecting of regularization parameters that maximize the performance is still an open question. In this paper, three data points of regularization parameters $(\log_{10}\lambda_x, \log_{10}\lambda_p)$ from simulation were fitted with a linear regression model. The three data points are $(-1, -2)$, $(-1.5, -2)$, and $(-1.5, -1.5)$, and the fitting is $2\log_{10}\lambda_x + \log_{10}\lambda_p = -4.5$. The regularization parameters for common carotid artery data set $(\lambda_x = 0.06, \lambda_p = 0.01)$ are on this line, but that of silica gel tube data set $(\lambda_x = \lambda_p = 0.11)$ is not. The reason is that the best regularization parameter setting was estimated through the simulation studies where the point spread function perfectly matches the RF signals, and the noise was assumed to be Gaussian. However, these conditions may not hold good in the real data, and hence the best setting tends to yield false layers formed by side lobes. For the common carotid artery data set, these false layers can be filtered out by an extra postprocessing [see Fig. 7(c) and (d)], while for the silica gel tube data set, these false layers could be reduced by large regularization parameters without any extra postprocessing.

REFERENCES

[1] M. Fatemi and A. C. Kak, "Ultrasonic B-scan imaging: Theory of image formation and a technique for restoration," *Ultrason. Imag.*, vol. 2, no. 1, pp. 1–47, 1980.

[2] J. Krautkrämer and H. Krautkrämer, *Ultrasonic Testing of Materials*. Berlin, Germany: Springer-Verlag, 1990.

[3] A. Ng and J. Swanevelder, "Resolution in ultrasound imaging," *Continuing Edu. Anaesthesia, Critical Care Pain*, vol. 11, no. 5, pp. 186–192, 2011.

[4] J. A. Jensen, "Estimation of pulses in ultrasound B-scan images," *IEEE Trans. Med. Imag.*, vol. 10, no. 2, pp. 164–172, Jun. 1991.

[5] T. Olofsson and T. Stepinski, "Minimum entropy deconvolution of pulse-echo signals acquired from attenuative layered media," *J. Acoust. Soc. Amer.*, vol. 109, no. 6, pp. 2831–2839, 2001.

[6] C. Yu, C. Zhang, and L. Xie, "A blind deconvolution approach to ultrasound imaging," *IEEE Trans. Ultrason., Ferroelect., Freq. Control*, vol. 59, no. 2, pp. 271–280, Feb. 2012.

[7] P. J. Huber, *Robust Statistics*. New York, NY, USA: Wiley, 1981.

[8] Z. Xu, "Data modeling: Visual psychology approach and $L_{1/2}$ regularization theory," in *Proc. Int. Congr. Math.*, Hyderabad, India, Aug. 2010, pp. 3151–3184.

[9] R. Lavarello, F. Kamalabadi, and W. D. O'Brien, "A regularized inverse approach to ultrasonic pulse-echo imaging," *IEEE Trans. Med. Imag.*, vol. 25, no. 6, pp. 712–722, Jun. 2006.

[10] A. Tuysuzoglu, J. M. Kracht, R. O. Cleveland, M. Çetin, and W. C. Karl, "Sparsity driven ultrasound imaging," *J. Acoust. Soc. Amer.*, vol. 131, no. 2, pp. 1271–1281, 2012.

[11] R. Tibshirani, "Regression shrinkage and selection via the lasso," *J. Roy. Statist. Soc. B (Methodol.)*, vol. 58, no. 1, pp. 267–288, 1996.

[12] M. Nikolova, "Local strong homogeneity of a regularized estimator," *SIAM J. Appl. Math.*, vol. 61, no. 2, pp. 633–658, 2000.

[13] E. J. Candès and T. Tao, "The Dantzig selector: Statistical estimation when p is much larger than n," *Ann. Statist.*, vol. 35, no. 6, pp. 2313–2351, 2007.

[14] Y. C. Eldar and G. Kutyniok, Eds., *Compressed Sensing: Theory and Applications*. Cambridge, U.K.: Cambridge Univ. Press, May 2012.

[15] D. L. Donoho and Y. Tsaig, "Fast solution of ℓ_1-norm minimization problems when the solution may be sparse," *IEEE Trans. Inf. Theory*, vol. 54, no. 11, pp. 4789–4812, Nov. 2008.

[16] B. Efron, T. Hastie, I. Johnstone, and R. Tibshirani, "Least angle regression," *Ann. Statist.*, vol. 32, no. 2, pp. 407–499, 2004.

[17] D. M. Malioutov, M. Cetin, and A. S. Willsky, "Homotopy continuation for sparse signal representation," in *Proc. IEEE ICASSP*, vol. 5. Philadelphia, PA, USA, Mar. 2005, pp. v/733–v/736.

[18] O. Michailovich and A. Tannenbaum, "Blind deconvolution of medical ultrasound images: A parametric inverse filtering approach," *IEEE Trans. Image Process.*, vol. 16, no. 12, pp. 3005–3019, Dec. 2007.

[19] H. Liebgott, R. Prost, and D. Friboulet, "Pre-beamformed RF signal reconstruction in medical ultrasound using compressive sensing," *Ultrasonics*, vol. 53, no. 2, pp. 525–533, 2013.

[20] C. Soussen, J. Idier, E. Carcreff, L. Simon, and C. Potel, "Ultrasonic non destructive testing based on sparse deconvolution," *J. Phys., Conf. Ser.*, vol. 353, no. 1, pp. 012018-1–012018-10, 2012.

[21] E. Carcreff, S. Bourguignon, J. Idier, and L. Simon, "A linear model approach for ultrasonic inverse problems with attenuation and dispersion," *IEEE Trans. Ultrason., Ferroelect., Freq. Control*, vol. 61, no. 7, pp. 1191–1203, Jul. 2014.

[22] T. Taxt and G. V. Frolova, "Noise robust one-dimensional blind deconvolution of medical ultrasound images," *IEEE Trans. Ultrason., Ferroelect., Freq. Control*, vol. 46, no. 2, pp. 291–299, Mar. 1999.

[23] R. Jiřík and T. Taxt, "Two-dimensional blind Bayesian deconvolution of medical ultrasound images," *IEEE Trans. Ultrason., Ferroelect., Freq. Control*, vol. 55, no. 10, pp. 2140–2153, Oct. 2008.

[24] S. S. Chen, D. L. Donoho, and M. A. Saunders, "Atomic decomposition by basis pursuit," *SIAM J. Sci. Comput.*, vol. 20, no. 1, pp. 33–61, 1998.

[25] N. Meinshausen, "Relaxed Lasso," *Comput. Statist. Data Anal.*, vol. 52, no. 1, pp. 374–393, Sep. 2007.

[26] E. van den Berg and M. P. Friedlander, "Probing the Pareto frontier for basis pursuit solutions," *SIAM J. Sci. Comput.*, vol. 31, no. 2, pp. 890–912, 2008.

[27] J. Duan, H. Zhong, B. Jing, S. Zhang, and M. Wan, "Discover layered structure in ultrasound images with a joint sparse representation model," in *Proc. IEEE Int. Ultrason. Symp.*, Taipei, Taiwan, Oct. 2015, pp. 1–4.

[28] A. Chambolle and P.-L. Lions, "Image recovery via total variation minimization and related problems," *Numer. Math.*, vol. 76, no. 2, pp. 167–188, 1997.

[29] A. V. Oppenheim and R. W. Schafer, *Discrete-Time Signal Processing*, 3rd ed. New York, NY, USA: Prentice-Hall, 2009.

[30] CVX Research Inc. (Aug. 2012). *CVX: MATLAB Software for Disciplined Convex Programming, Version 2.0*. [Online]. Available: http://cvxr.com/cvx

[31] M. C. Grant and S. P. Boyd, "Graph implementations for nonsmooth convex programs," in *Recent Advances in Learning and Control* (Lecture Notes in Control and Information Sciences), V. D. Blondel, S. P. Boyd, and H. Kimura, Eds. Berlin, Germany: Springer-Verlag, 2008, pp. 95–110.

[32] T. Taxt, "Restoration of medical ultrasound images using two-dimensional homomorphic deconvolution," *IEEE Trans. Ultrason., Ferroelect., Freq. Control*, vol. 42, no. 4, pp. 543–554, Jul. 1995.

[33] O. V. Michailovich and A. Tannenbaum, "Despeckling of medical ultrasound images," *IEEE Trans. Ultrason., Ferroelect., Freq. Control*, vol. 53, no. 1, pp. 64–78, Jan. 2006.

[34] P. Pignoli, E. Tremoli, A. Poli, P. Oreste, and R. Paoletti, "Intimal plus medial thickness of the arterial wall: A direct measurement with ultrasound imaging," *Circulation*, vol. 74, no. 6, pp. 1399–1406, Dec. 1986.

[35] E. de Groot *et al.*, "Measurement of carotid intima–media thickness to assess progression and regression of atherosclerosis," *Nature Rev. Cardiol.*, vol. 5, no. 5, pp. 280–288, 2008.

[36] J. H. Stein *et al.*, "Use of carotid ultrasound to identify subclinical vascular disease and evaluate cardiovascular disease risk: A consensus statement from the American Society of Echocardiography carotid intima-media thickness task force endorsed by the society for vascular medicine," *J. Amer. Soc. Echocardiogr.*, vol. 21, no. 2, pp. 93–111, 2008.

Junbo Duan (M'15) received the B.S. degree in information engineering and the M.S. degree in communication and information system from Xi'an Jiaotong University, Xi'an, China, in 2004 and 2007, respectively, and the Ph.D. degree in signal processing from Université Henry Poincaré, Nancy, France, in 2010.

He was a Postdoctoral Fellow with the Department of Biomedical Engineering and Biostatistics & Bioinformatics, Tulane University, New Orleans, LA, USA, until 2013. He is currently an Assistant Professor with the Department of Biomedical Engineering, Xi'an Jiaotong University. His current research interests include probabilistic approaches to inverse problems in biomedical engineering and bioinformatics.

Hui Zhong received the B.S. and Ph.D. degrees in biomedical engineering from Xi'an Jiaotong University, Xi'an, China, in 2000 and 2006, respectively.

She is currently a Lecturer with the Department of Biomedical Engineering, Xi'an Jiaotong University. Her current research interests include medical ultrasound imaging and its application for HIFU.

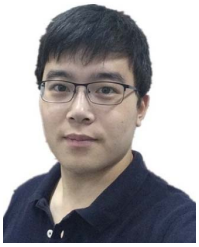

Bowen Jing was born in Gansu, China, in 1989. He received the B.S. degree in biomedical engineering from Xi'an Jiaotong University, Xi'an, China, in 2011, where he is currently pursuing the Ph.D. degree with the Department of Biomedical Engineering.

His current research interests include ultrafast ultrasound imaging, ultrasound beamforming, and motion estimation.

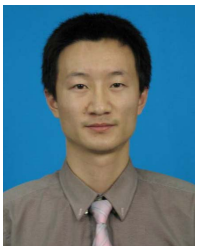

Siyuan Zhang received the B.S. and Ph.D. degrees from the Department of Biomedical Engineering, Xi'an Jiaotong University, Xi'an, China, in 2004 and 2009, respectively.

He is currently an Associate Professor with the Department of Biomedical Engineering, Xi'an Jiaotong University. His current research interests include the development of novel ultrasonic imaging techniques and therapeutic methods, and more notably, in areas of the guidance and monitoring of thermal ablation with acoustic radio-frequency signals.

Mingxi Wan (M'01) was born in Hubei, China, in 1962. He received the B.S. degree in geophysical prospecting from the Jianghan Petroleum Institute, Jingzhou, China, in 1982, and the M.S. and Ph.D. degrees in biomedical engineering from Xi'an Jiaotong University, Xi'an, China, in 1985 and 1989, respectively.

From 1995 to 1996, he was a Visiting Scholar and an Adjunct Professor with Drexel University, Philadelphia, PA, USA, and Pennsylvania State University, State College, PA, USA. From 2000 to 2001, he was a Visiting Scholar with the Department of Biomedical Engineering, University of California at Davis, Davis, CA, USA. From 2000 to 2010, he was the Dean of the School of Life Science and Technology, Xi'an Jiaotong University, where he is currently a Full Professor with the Department of Biomedical Engineering. He has authored or coauthored over 100 peer-reviewed publications in international journals and five books about medical ultrasound. His current research interests include voice science, ultrasonic imaging, especially in tissue elasticity imaging, contrast and tissue perfusion evaluation, therapeutic ultrasound, and theranostics.

Dr. Wan was a recipient of several important awards from the Chinese government and university.